Field-driven athermal activation of amorphous metal oxide semiconductors for flexible programmable logic circuits and neuromorphic electronics

Kulkarni, Mohit Rameshchandra; John, Rohit Abraham; Tiwari, Nidhi; Nirmal, Amoolya; Ng, Si En; Nguyen, Anh Chien; Mathews, Nripan

2019

Kulkarni, M. R., John, R. A., Tiwari, N., Nirmal, A., Ng, S. E., Nguyen, A. C., & Mathews, N. (2019). Field-driven athermal activation of amorphous metal oxide semiconductors for flexible programmable logic circuits and neuromorphic electronics. Small, 15(27), 1901457-. doi:10.1002/smll.201901457

https://hdl.handle.net/10356/138083

https://doi.org/10.1002/smll.201901457

Field-Driven Athermal Activation Of Amorphous Metal Oxide Semiconductors For Flexible Programmable Logic Circuits And Neuromorphic Electronics

*Mohit Rameshchandra Kulkarni[1], Rohit Abraham John[1], Nidhi Tiwari[2], Amoolya Nirmal[1], Si En Ng[1], Anh Chien Nguyen[1], Nripan Mathews[1,2]**

[1] School of Materials Science and Engineering, Nanyang Technological University, 50 Nanyang Avenue, Singapore 639798

[2] Energy Research Institute @ NTU (ERI@N), Nanyang Technological University, Singapore 637553

* Corresponding author

Prof. Nripan Mathews (Email: Nripan@ntu.edu.sg)

Keywords: field-driven athermal activation, amorphous metal oxides, programmable logic circuits, neuromorphic electronics

Abstract:

Despite extensive research efforts, large-scale realization of metal oxide-based transparent and flexible electronics is still impeded by high-temperature deposition and post-annealing processes, incompatible with flexible substrates. Ideally an athermal treatment modifying the electronic structure of amorphous metal oxides to generate sufficient carrier concentration, would help mitigate such high-temperature processing requirements, enabling realization of high-performance electronics on thermally-fragile flexible substrates. Here, we demonstrate a novel field-driven athermal activation of amorphous metal oxide semiconducting channels via an electrolyte/ionic liquid (IL) gating approach. Facilitating migration of charged oxygen species across the semiconductor-dielectric interface, this approach modulates the local electronic structure of the semiconducting channel, generating sufficient carriers for charge transport and activating oxygen-compensated thin films without the need of high-temperature processing. The thin-film transistors investigated in this work depicted an enhancement of the ionic-gated linear mobility from 51 to 105.25 cm^2/Vs and back gated mobility from 8.09 cm^2/Vs to 14.49 cm^2/Vs, by creating additional oxygen vacancies. The accompanying stochiometric transformations, monitored via spectroscopic measurements (XPS) corroborate the detailed electrical (TFT, current-evolution) parameter analyses, providing critical insights into the underlying oxygen vacancy generation mechanism and clearly demonstrating electrolyte-gated field-induced activation as a promising alternative to conventional high-temperature annealing strategies. By facilitating an on-demand active programming of the operation modes of transistors (enhancement vs depletion), this technique paves way for facile fabrication of logic circuits and neuromorphic transistors for bio-inspired computing.

Introduction:

With a highly hybridized conduction band minima (CBM) insensitive to local structural randomness, amorphous semiconducting oxides of post transition metals [indium (In), gallium (Ga), tin (Sn), and zinc (Zn)] are superior alternatives to a-Si:H, poly-Si and organic semiconductors for applications that demand high-mobility, transparency, flexibility, and large-area uniformity.[1,2] However, the high-temperature deposition and post-annealing processes required for high-mobility activation in these oxide semiconductors impede its realization on thermally-fragile flexible substrates, entailing significant research efforts in this direction.[3] The electrical transport properties of amorphous metal oxide semiconductor

(AMOS) thin films have been reported to hinge on its local electronic structure, which in turn depends on their oxygen stoichiometry.[2,4] In this regard, compositional screening[5,6] and vacancy engineering[7] strategies have been undertaken in both vacuum- and solution-based routes to hit the stochiometric sweet spot, but demand tedious and expensive controls over the deposition conditions. Thermal post-annealing techniques offer a facile approach to tune the oxygen vacancy concentration in such oxides, but often require high temperatures incompatible with flexible substrates.[8] Recent strategies adopted to reduce the thermal budget include tuning precursor formulations to enable combustion chemistry[9,10] and alternate annealing techniques like ultraviolet photochemical activation.[11,12] While combustion chemistry enables processing at temperatures lower than 200°C, it requires a careful selection of metal salts, fuels and stabilizers to ignite the desired reaction.[9,10] Ultraviolet photochemical activation is more promising this regard[12], but utilizes high-power irradiation often in a controlled N_2 ambient[11], hampering large-scale fabrication on flexible polymer substrates. Ideally an athermal treatment optimized to modify the local electronic structure of AMOS to generate sufficient carriers for charge transport, would ensure high-mobility devices at room temperature, overcoming conventional high-temperature processing challenges.

Application of high electric fields have been shown to trigger both electrical and structural transitions in a wide variety of materials. These include insulator-metal/ Mott transitions [13–15] and electric field induced structural changes in VO_2 [16], $MoTe_2$ [17] and $SrCoO_{2.5}$ [18]. In many of these cases, application of the high electric field was enabled through the formation of an electrical double layer (EDL) utilising either ionic liquids.[19,20] The EDL generates an extremely high electrostatic field of ~ 50 MV/mm[21] which have been shown to be capable of moving ions in/out of solid films, eg. $SrTiO_3$.[13,14] Electric field-driven migration and creation of oxygen vacancies is also well-established in the resistive switching community, defining the switching characteristics in memristive devices. [22,23]

Inspired from these previous advances and recent reports on electric field induced TFT modulation [24,25], we adopt a novel field-driven electrolyte/ionic liquid gating approach to athermally modulate the local electronic structure of AMOS, favourably tuning the oxygen-stoichiometry at room temperature. The electrolyte acts as a permeable membrane for oxygen extraction/intercalation from/into the semiconducting channel, modulating the available carriers for charge transport on demand, thereby activating oxygen-compensated thin films at room temperature. Optimized biasing conditions (function of the bias amplitude, duration,

initial carrier concentration and measurement ambient) enable fabrication of high-mobility (> 100 cm^2/V s) sputtered indium tungsten oxide (IWO) thin film transistors (TFTs) on flexible polyimide substrates, mitigating high-temperature post-annealing processes. Detailed electrical and spectroscopic characterizations provide novel insights into the mechanism of field-driven migration of oxygen vacancies, comprehensively establishing this technique as a promising alternative to conventional high-temperature processing. On-demand programming of operation modes (enhancement and depletion) is also demonstrated without any additional fabrication steps, facilitating facile realisation of logic circuits and neuromorphic transistors.

Results and Discussion:

With lower operational voltages, higher mobility and a better resistance to moisture and acidic environments, indium tungsten oxide (IWO) thin films are promising alternatives to the intensively-researched indium gallium zinc oxide (IGZO) counterparts, justifying their selection as the reference prototypical AMOS system for this study.[26] Akin to other AMOS, the oxygen stoichiometry-dependent transport properties enable probing of the local electronic structure via techniques that alter the oxygen vacancy concentration in such films.[27] Although a higher oxygen dissociation energy for W-O (653 kJ/mol) when compared to In-O (360 kJ/mol), Zn-O (284 kJ/mol) and Ga-O (285 kJ/mol), makes oxygen vacancy formation challenging, it nevertheless provides a good benchmark for such AMOS thin films. [28].

To investigate the field-driven vacancy creation effects, the devices were configured in a double-gated field-effect transistor (FET) configuration with EMIM TFSI (1-Ethyl-3-methylimidazolium bis(trifluoromethylsulfonyl)imide) and SiO_2 serving as the top and bottom gate dielectrics respectively (Figure 1a). The top gate served as the main field-application terminal, while the bottom gate probed the electronic structure of the semiconducting channel as detailed in further sections. Device fabrication and physical characterizations are described in detail in the methods section and Supporting-Information Figure S1. Figure 1b-e depicts the transfer and output characteristics of the devices in both the top and bottom-gated configurations.

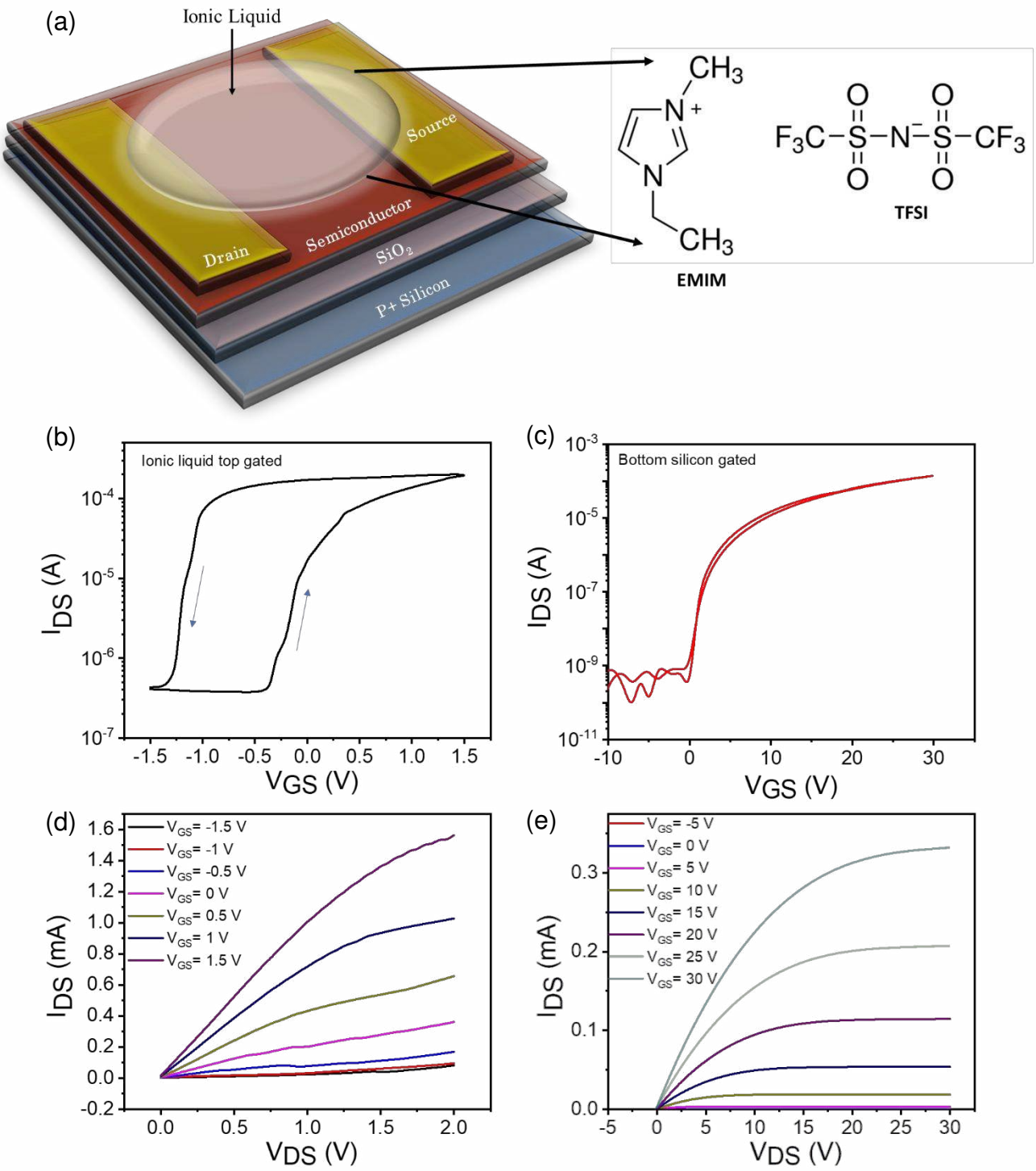

Figure 1 (a) shows the double-gated FET configuration with EMIM TFSI (1-Ethyl-3-methylimidazolium bis(trifluoromethylsulfonyl)imide) and SiO_2 serving as the top and bottom gate dielectrics respectively. (b-e) depicts the transfer and output characteristics of devices in the top (b, d) (V_{DS} of 0.3V) and bottom-gated configurations (c, e) (V_{DS} of 5V) respectively.

The linear field-effect mobilities were extracted from the transfer characteristics using the equation $\mu = [\delta I_d/\delta V_g] \times [L/WC_iV_d]$ where L is the channel length (150 μm), W is the channel width (1000 μm) and C_i is the gate dielectric capacitance. The mobility was calculated to be around 8 $cm^2V^{-1}s^{-1}$ for the bottom electronic-gated mode, and 51 $cm^2V^{-1}s^{-1}$ for the top ionic-gated mode. For EMIM TFSI, a capacitance value of 2 $\mu F/cm^2$ @ 20 Hz [29] was utilised for mobility calculations. The large electrical-double-layer (EDL) capacitance resulted in efficient carrier accumulation within the small electrochemical window of the ion liquid, resulting in an ultralow voltage and power operation. Devices in the electronic back-gated mode clearly depicted a negligible clockwise hysteresis, while the ionic top-gated mode exhibited a larger anticlockwise hysteresis window of 1 V. In the ionic top-gated mode, the anticlockwise hysteresis was attributed to migration-relaxation kinetics of mobile ions in the dielectric,.[31] Forward scan resulted in migration of cations towards the ionic liquid-semiconductor interface, accumulating electrons in the IWO layer to form a conductive channel. This resulted in lower voltage requirements for the subsequent channel formation in the reverse scan, accounting for the anticlockwise hysteresis.

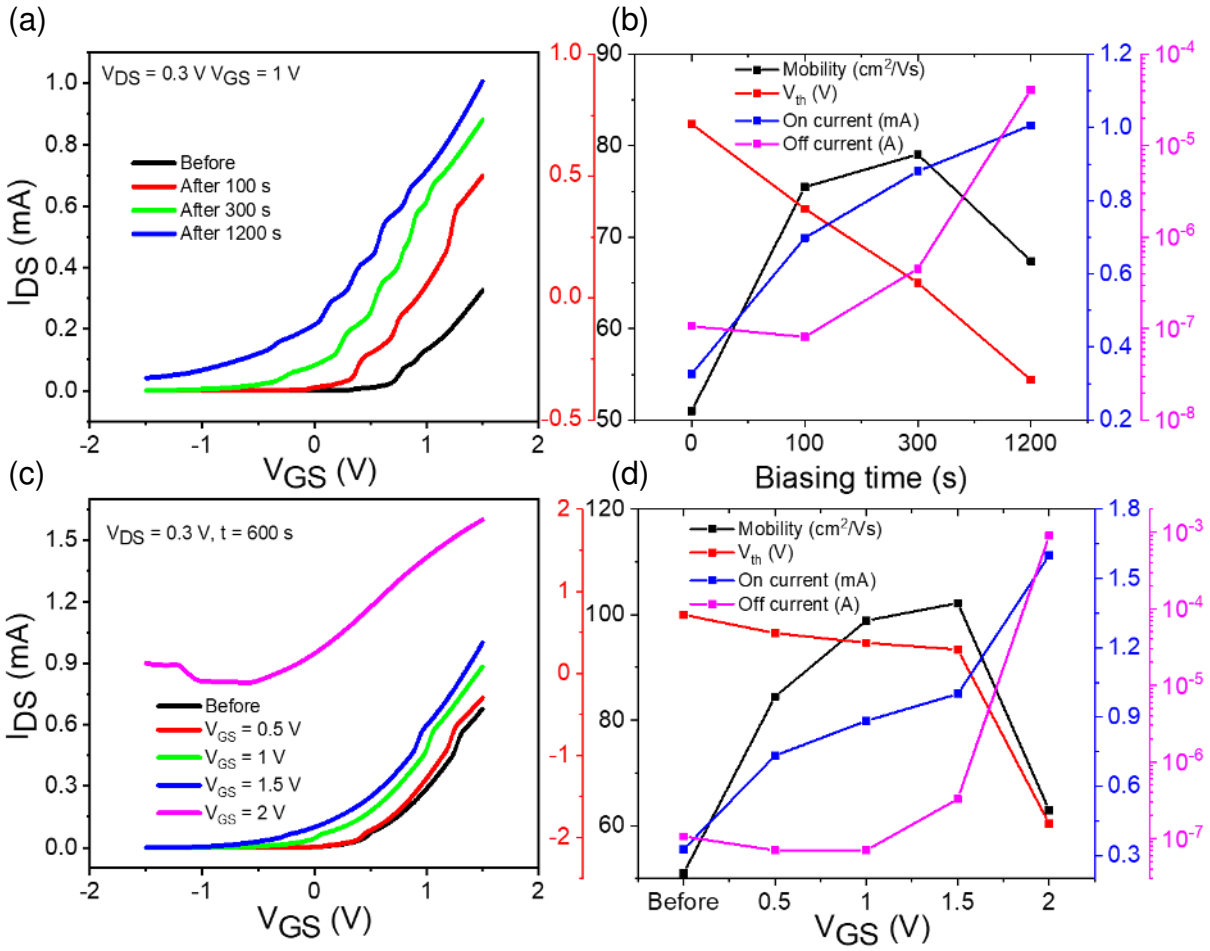

Figure 2 (a, c) depicts the transfer characteristics of the transistors subjected to various dosages of electric field (time and biasing voltage respectively) in the top-gated configuration.(b, d) summarizes the shift of mobility, threshold voltage, I_{on} and I_{off} as a function of the bias time and voltage respectively.

To systematically examine field-driven vacancy creation, the devices were initially biased in the ionic top-gated configuration with the bottom-gate floated. To simplify the analysis, only the forward sweeps of the transfer characteristics were taken into consideration. Constant positive biasing of the ionic top-gate at 1 V for 1200 seconds resulted in a negative shift of the threshold voltage (V_{th}) from 0.72 V to -0.34 V and higher off (I_{off}) and on-currents (I_{on}), indicating generation of excess carriers for charge transport or passivation of trap states at the electrolyte-semiconductor interface (Figure 2a). The gate leakage currents were carefully recorded to eliminate possible gate-screening effects and was observed to be around 100 nA for all of the devices studied (see Figure S2 in the Supporting Information). Biasing with higher fields or longer durations resulted in a further programmed shift of V_{th}, I_{on} and I_{off}, confirming this observation. Figure 2a depicts the shift in the transfer characteristics of ionic top-gated IWO TFTs, recorded immediately after 100 s, 300 s and 1200 s of application of the electric field (V_{GS}= 1 V, V_{DS} = 0.3 V). The shift in mobility, V_{th}, I_{on} and I_{off} are summarized in Figure 2b. The values of V_{th} were extracted from the linear fit in I_{ds} versus V_{gs} curves in the linear region. The increase in I_{on} resulted in higher mobilities. The devices depicted an increase in field-effect mobility from 51 $cm^2/V^{-1}s^{-1}$ to 105 $cm^2/V^{-1}s^{-1}$ for bias applications up to 1.5 V and 600 seconds. Effect on transfer characteristics due to variation in drain voltage, at constant gate bias voltage of 1V is shown in figure S3.

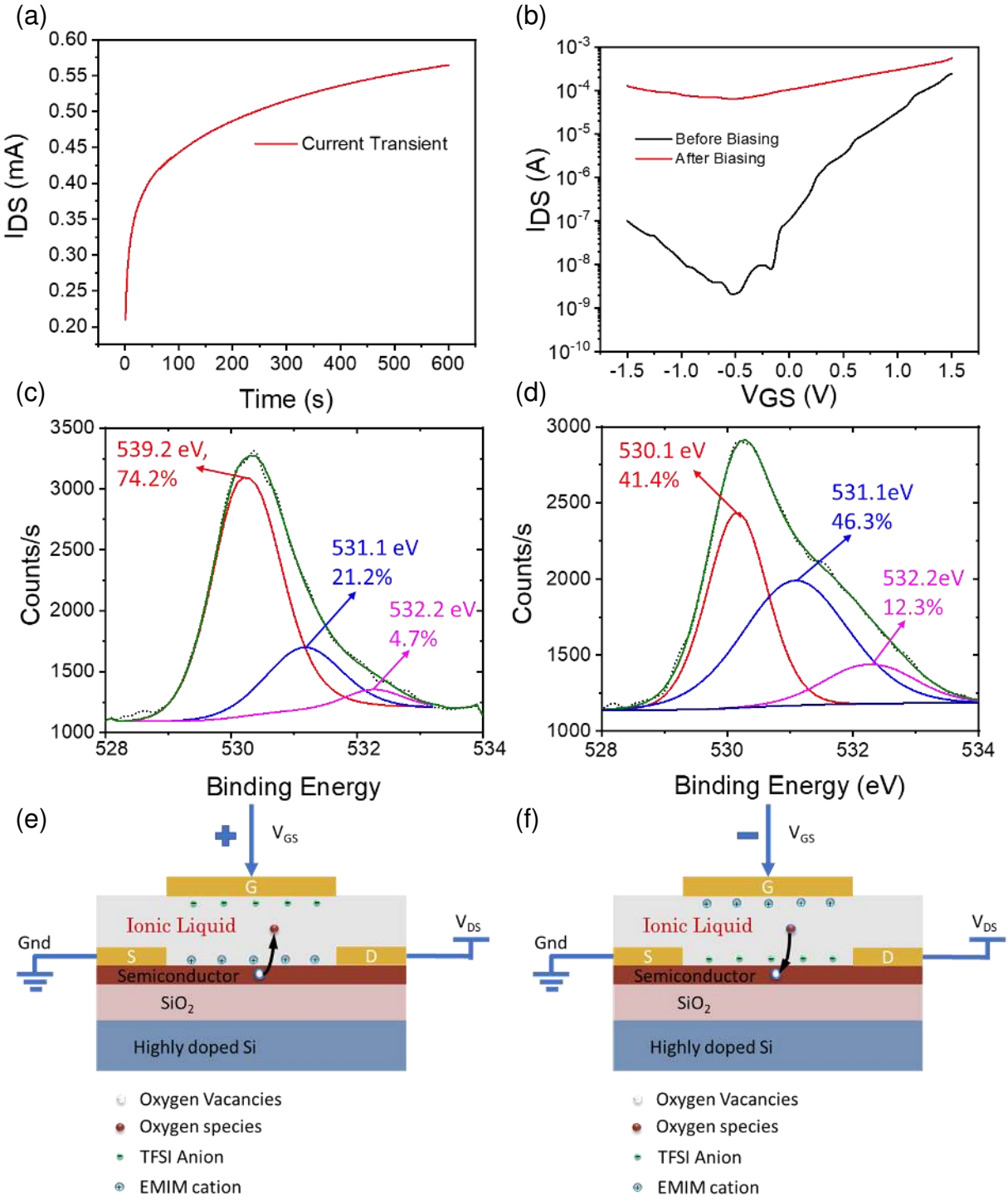

Figure 3 (a) current transient for 600s of gate biasing voltage of 1 V and drain voltage of 0.3V (b) top-gated FET characteristics of devices, post application of the electric field V_{GS} = 1V. (c) XPS of untreated sample (d)XPS after ionic liquid treatment (e) Mechanism explaining creation of oxygen vacancy with application of positive gate voltage (f) Mechanism for dissociation of oxygen vacancy with application of negative gate voltage.

Current transient measurements were next recorded under a constant electric field to get more insight into the underlying mechanism (Figure 3a). Figure 3b shows the corresponding transfer characteristics before and after biasing. Upon bias application, the drain current first increased

rapidly followed by gradual saturation, indicating the presence of two possible processes under play. Under a bias of +1 V, the I_{ds} increased from 0.21 mA to 0.35 mA in 18 seconds, followed by a gradual saturation to 0.565 mA for bias durations greater than 600 seconds. To get a more direct evidence of the underlying mechanism, XPS measurements were performed and analysed for the metal-oxygen bonding (Figure 3c,d). Since the conduction pathways in these oxides are predominantly dictated by vacant spatially dispersed ns orbitals, the O 1s peak was analysed to estimate the modulation of oxygen vacancies. The O 1s peak was deconvoluted to three individual peaks located around 530.1, 531.1, and 532.2 eV.[12] The peak at the lowest binding energy (~ 530.1 eV) was assigned to the oxygen atoms in the fully oxidized indium environment (lattice oxygen; M−O−M). The mid-peak at ~ 531.1 eV was assigned to oxygen ions in the oxygen-deficient region (indicative of oxygen vacancy concentration). And the peak at high binding energy (~ 532.2 eV) was assigned to the presence of loosely bound oxygens (adsorbed oxygen) associated with the presence of hydroxyl groups on the surface.[32] The percentage area of M-O-M peak, oxygen vacancy peak and adsorbed oxygen peak was changed from 74.2% to 41.4%, from 21.2% to 46.3%. from 4.7% to 12.3% respectively. XPS analyses revealed an increase in the concentration of oxygen vacancies for thin films that were biased at +1 V for 1200 seconds, authenticating the current transient measurements and hypothesis of oxygen vacancies modulation using the high electric field present due to EDL at interface of the ionic liquid and channel. Films biased at lower dosages (1V, 15 s) did not show any difference in the M-O bonding in the XPS analyses (data not shown). Hence, the initial rapid increase in the current transients was attributed to the passivation of defects/trap centres like surface-adsorbed moisture/oxygen at the electrolyte-semiconductor interface, which may not alter the carrier concentration of the semiconducting channel permanently.

From our data (displayed in figure 2, 3 and S4), the modulation of oxygen vacancies is evident in terms of the shift in threshold voltage and increase in on-state current in the transfer characteristics curve of ionic liquid gated thin film transistor. Based on these observations we propose that upon positive bias application, defects/traps due to surface adsorbates get passivated rapidly by the ionic liquid causing the initial surge in the channel current for a given electric field. Prolonged application of this electric field facilitates extraction of oxygen (creation of oxygen vacancies) from the semiconducting lattice to generate additional carriers for charge transport, resulting in a permanent shift of V_{th} and an increase in I_{on} (Figure 3e). Higher electric fields accelerate this extrusion process, shifting the V_{th}, I_{on} and I_{off} by larger

amounts. Application of electric field in the opposite direction (negative biasing) intercalates oxygen back into the semiconducting channel (Figure 3f) and should shift the electrical parameters back towards the original state. Analysis of this reverse process via detailed TFT characterizations indicate a higher barrier for reverse process as compared to the extrusion (Figure S4). This signifies that it is easier to remove the oxygen species than to reintroduce them back into the film matrix. The observed disparity may be explained as follows. On the application of a positive bias, the surface adsorbed oxygen species on the channel layer are removed initially followed by the oxygen species from the matrix of thin film. Desorption of the surface oxygen species is a fairly facile process, thus requiring a relatively shorter duration of positive bias to achieve desired level of carrier concentration. However, application of negative bias to return the oxygen species from the ionic liquid to the film is a more tedious process. This can be attributed to the low concentration of dissolved oxygen species in the ionic liquid. Comparative measurements were carried out under vacuum, N_2, Ar and dry air ambient to unravel the dependencies (Figure S5). The rate of vacancy creation was observed to be maximum under vacuum conditions. Introduction of N_2 and Ar decreased the extraction rate marginally and it was a minimum under dry air (N_2:O_2 = 80:20 by volume) conditions probably due to the oxygen saturation of ionic liquid and lack of an oxygen gradient. These results unravelled the effects of the number of readily available oxygen atoms to aid this diffusion process. Presence of an oxygen gradient (due to the oxygen-deficient surrounding) maximized the vacancy creation effects. Dry air probably diffused and saturated the ionic liquid with O_2, decreasing its effectiveness as an oxygen-extractor. However, the presence of readily available oxygen enhanced the intercalation rate under dry air conditions (Figure S4, violet color) with the threshold voltage shifting back in the original direction after biasing of -1V for 1200sec.
The rate of the diffusive mechanism also varied as a function of the initial off channel current (indicating initial oxygen stoichiometry). The initial oxygen stoichiometry of these films was purposefully engineered for this study by varying the oxygen partial pressure during sputtering (total pressure was kept constant at 5 mTorr and oxygen partial pressure varied by modulating the flow rate- 1, 2 and 3 SCCM). Channels with a low initial carrier concentration depicted maximum shift in the evaluated electrical parameters in line with the previous observations. Figure S6 depicts the normalized change in I_{on} as a function of oxygen partial pressure at the time of deposition at constant magnitude and duration of application of the electrical field.

Back gated FET measurements were conducted subsequent to the IL field-induced activation process. All traces of the ionic liquid were washed away prior to these measurements to prevent

further oxygen-getting reactions for a fair analysis. Figure S7 depicts the back-gated FET characteristics of devices, post application of the electric field. The unchanged back-gated transfer characteristics for IL field voltages of 1 V and duration 15 seconds supported the proposed hypothesis of surface defect passivation during the initial stages. However, prolonged (800 s blue curve in S7) electric fields resulted in a shift of electrical parameters (V_{th}, I_{on}) for even the back-gated channels with an enhancement in mobility from 8cm^2/Vs to 14.49cm^2/Vs, re-validating the saturation in current transient measurements, and increased oxygen vacancy generation as reflected by the XPS measurements.

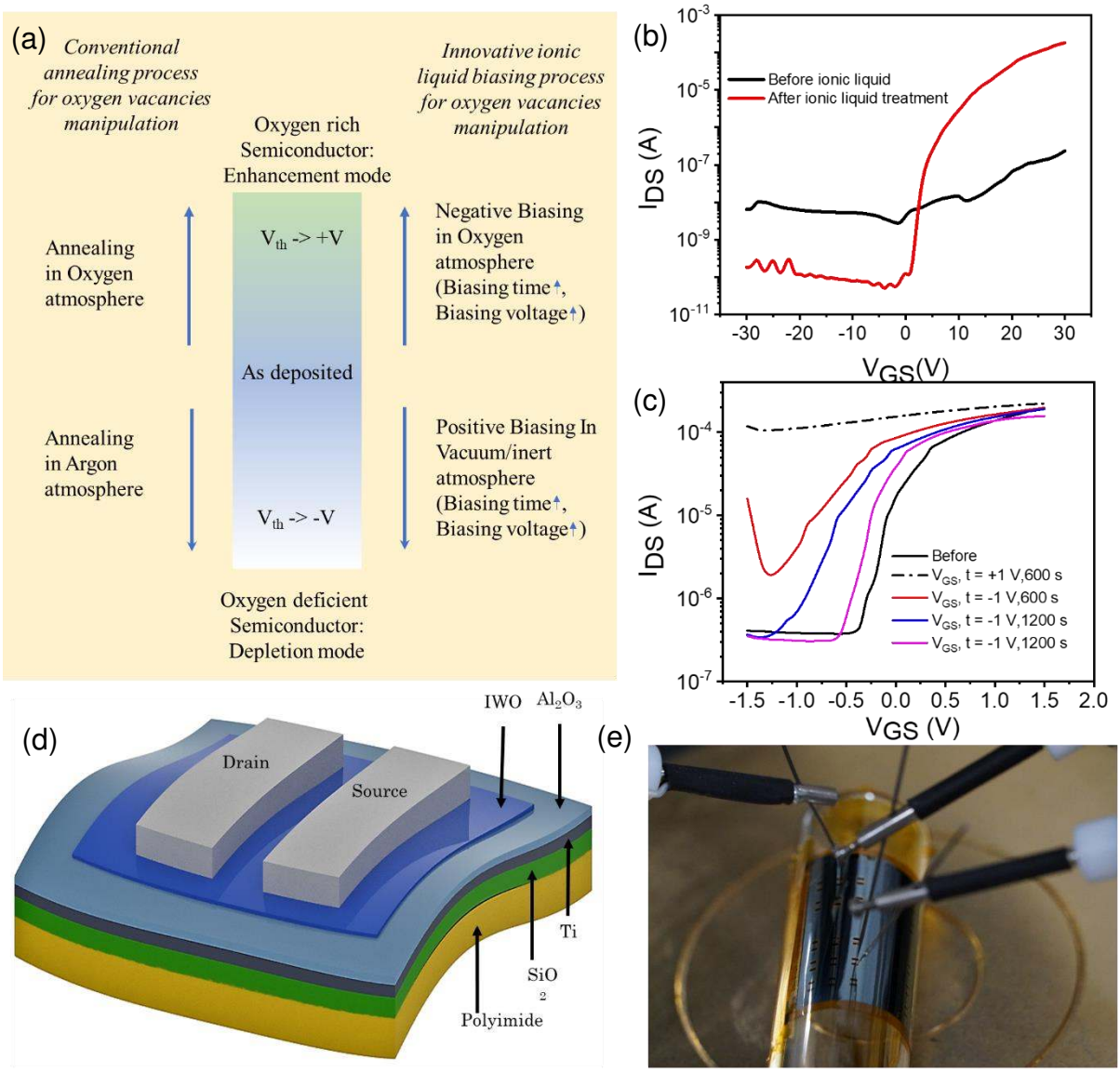

Figure 4 (a) Comparison between conventional vs ionic liquid biasing for oxygen vacancies modulation. (b)Activation of not working bottom contact thin film transistor, V_{DS} of 10V (c) Reversible transfer characteristics of Ionic liquid based flexible thin film transistor with applied electric field. Black solid line indicates original transfer characteristics, dotted black line indicates transfer characteristics after biasing of 1V for 600sec in vacuum, the red line represents transfer characteristics after 600 s in vacuum, blue line corresponds to transfer characteristics after biasing for 1200 s in vacuum and magenta line corresponds to transfer characteristics after 1200 s biasing in synthetic air

on the same device. (V_{DS} =0.3V) (d) structure of flexible thin film transistor, (e) Fabricated flexible TFT mounted on curved surface of 1.5cm diameter.

Thus, in this work, the claim of field-driven oxygen vacancy generation is supported through systematic electrical parameter analyses and spectroscopic measurements. Figure 4 (a) compares the conventional annealing parameters with EDL annealing parameters to modulate oxygen vacancies. To demonstrate the ultimate use of this approach as an alternative to conventional high-temperature deposition and annealing strategies in order to modulate device parameters using the EDL gating technique the possibility of activating a non-functional transistor was demonstrated in Figure 4(b) (with 1V biasing voltage applied for 40min). It can be clearly seen that the initially non-functioning TFT (black) was activated to a working transistor with mobility of 7.1 $cm^2V^{-1}s^{-1}$ and on-off ratio of 10^6. As indicated previously, the high temperatures required to access high performance in oxide semiconductors makes it incompatible with plastic substrates. Thus, efforts to modulate the local electronic structure and oxygen stoichiometry of oxygen-compensated thin films deposited on flexible polyimide substrates were also made. Thin films of IWO were sputtered under same conditions used for Silicon substrates on 130nm Al_2O_3 (deposited via Thermal atomic layer deposition) with Titanium metal as gate electrode. Al_2O_3 and EMIM TFSI served as the bottom and top gate dielectrics respectively (structure of flexible TFT, Figure 4d,e). Application of electric field (1 V, 600 seconds) generated additional carriers in the channel, resulting in depletion mode devices. The devices could be brought back close to its original state by biasing in synthetic air. The transfer characteristics are shown in figure 4c.

By creating additional oxygen vacancies in the semiconducting channel, this field-driven approach also enables selective activation and programming of TFTs to enhancement and depletion-modes in an on-demand manner, paving way for facile realization of logic circuits like inverters without additional fabrication steps. To demonstrate this, an array of 6 X 6 IWO TFTs (figure 5a) were sputtered on a 2.5x2.5 cm^2 SiO_2 substrate (bottom) and the ionic liquid was top gated in a drop on-demand manner (on TFTs shown in yellow color) and biased with positive voltage to create oxygen vacancies and form a depletion mode TFT. Figure 5b displays transfer characteristics of this depletion mode TFT and the original enhancement mode TFT. All the transistors depicted comparatively low carrier concentration in their back-gated channel before the field-driven activation process. The 1st column of transistors were allowed to remain in the enhancement mode, while the next column was programmed to the depletion mode by

biasing 1 V for 800 seconds. The mobility and V_{th} of one of the these back gated enhancement devices were 8.09 cm^2/Vs and 11.81 V respectively while that for depletion devices were 14.49 cm^2/Vs and -2.11 V respectively. Conventional thermal annealing strategy is a global annealing technique that does not allow for selective activation. Fabricating depletion mode and enhancement mode transistors on the same substrate would need separate deposition and masking steps which can be avoided using the present approach. This active on-demand programmability of the operation mode of transistors facilitated facile fabrication and tuning of logic circuits like inverters. To demonstrate this, ionic gated inverters were fabricated here via a single-step sputtering process. Prior to the field-activation process, both the load and driver transistors depicted an enhancement-mode operation with V_{on} around 0 V. The load transistors were then subjected to electric fields of 1 V for 600 s to induce additional carriers in the channel shifting the V_{on} negative. With its promising electrical performance, the ionic gated transistor was used in the fabrication of a double enhancement mode TFT inverter, for possible application in logic gates. Figure 5d shows the schematic of a double enhancement mode TFT inverter. In this mode, the top TFT works as a load to limit the current flowing through the bottom TFT. When positive voltage is applied to the bottom TFT, it turns on, shunting the output terminal to ground (state zero). When supplied with a negative voltage (state zero) the TFT is in off state allowing current to pass through the output terminal (state one), thus inverting the input.

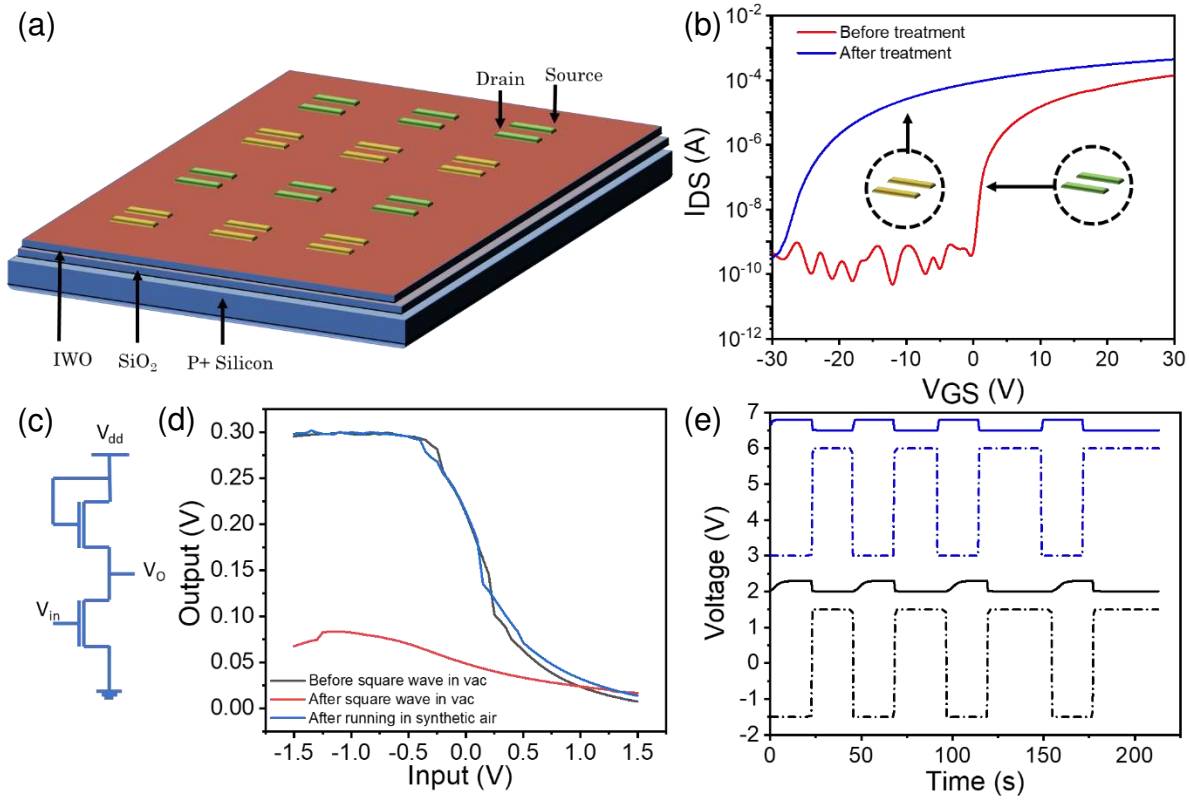

Figure 5 (a) Array of 6 X 6 IWO backgated TFTs made into row-wise on demand depletion and enhancement TFTs (b) Transfer characteristics of on demand depletion and enhancement TFTs in the array. V_{DS} of 5 V. (c) Schematic illustration of inverter using n-type thin film transistor (d) The static voltage inverter characteristics realized with ionic liquid biasing for different conditions. The black line corresponds to original inverter characteristics. The red curve is inverter characteristics after operating inverter in vacuum with square wave. The blue curve shows the repaired characteristics of same device after operating it in synthetic air with square wave. (e) stacked graphs of Output characteristics of inverter with square wave as input in synthetic air vs vacuum. The dotted (solid) black curve is the input (output) square wave in the vacuum. And the dotted (solid) blue curve is the input (output) square wave in the synthetic air.

Figure 5d demonstrates the static voltage transfer characteristics of the inverter with V_{DS} of 0.3V. Due the high electric field imposed by the ionic liquid, on application of voltage, the oxygen vacancies vary, resulting in degradation of the inverter transfer characteristics. Figure 5b shows the initial transfer characteristics in a vacuum with a gain of 0.61, that gets severely degraded to a gain of 0.09 after a square wave is run for 200s from this inverter. However, with the introduction of dry air and a repeat of square wave measurement, this degradation is reversed and the original transfer characteristics with a gain around 0.61 is recovered. Another important characterization parameter for an inverter is its output characteristics. Figure 5e shows the output characteristics of the inverter with a square wave as input in synthetic air vs vacuum environment. It can be noted from the figure that the rise time and fall time is faster when operating in synthetic air. This can be attributed to the change in V_{th} due to variation of surface adsorbed oxygen on IWO as the interstitial oxygen species manipulation is relatively

slow process and it may not be able to react to a fast change occurring with square wave input. A constant current flowing through the bottom TFT in the vacuum environment for a longer duration, results in increased carrier concentration due to decrease in the oxygen concentration on the surface of IWO causing the negative V_{th} shift. The negative V_{th} shift of the bottom TFT does not allow the transistor to switch off completely, leading to the sluggish response. However, in synthetic air, the variation of carrier concentration is hugely suppressed because of the higher concentration of oxygen already present in the atmosphere of the synthetic air compared to vacuum. This is in agreement with the decrease in oxygen vacancy variation observed in the case of constant biasing applied in synthetic air (Figure S5). Hence, operating ionic gated transistors in synthetic/oxygen environment might be beneficial for stability and faster rise and fall time (supporting figures S8 a and b shows comparison between input output characteristics of inverter in vacuum vs synthetic air depicting sharper turn off in synthetic air operation than in vacuum operation). The superior operation of the ionic liquid gated inverter in synthetic air can be attributed to the V_{th} stability of the bottom ionic liquid gated transistor characteristics while in operation.

As a final demonstration of the utility of this field-driven oxygen vacancy generation approach, neuromorphic transistors with programmable plasticity were realised in a comprehensive manner, correlating the above explanations with weight plasticity. Very recently, electrolyte-gated FETs have been extensively researched for hardware emulation of biological signal-processing.[29,33] Contrary to mass storage and conventional logic operations, emulation of biological signal-processing set unique requirements on the hardware switching devices, namely- a strong operational history, analog (non-abrupt) switching transitions, continuously distributed conductance states and programmable plasticity.[34] Although two-terminal memristive solutions have dominated this research area, three-terminal FET-based solutions have recently received significant scientific attention in this regard.[35–37] With a gated control of channel conductance exploiting time-dependent hysteresis and programmable shifts of threshold voltage (V_{th}), the thin-film transistor (TFT) configuration is promising in achieving programmable plasticity, compatible with spike-based computing algorithms.[35] Here, we harness the hysteresis and field-driven oxygen-getting ability of electrolyte-gated TFTs to demonstrate volatile and non-volatile switching characteristics, emulating short and long-term plasticity features respectively. Electrostatic doping due the large EDL capacitance caused volatile switching of memory states, accounting for short-term plasticity features, while the field-driven extrusion/intercalation of charged oxygen species created non-volatile changes in

channel conductance, accounting for long-term plasticity features. Ionic migration-relaxation kinetics in the ionic liquid mimicking Ca^{2+} influx in dendritic spines modulated the electronic conductance-state of the semiconducting channel, while charge transport pathways emulated the synaptic cleft, and channel-conductance defined the synaptic weight. The pre- and post-synaptic potentials at the gate and source terminals tuned the post-synaptic channel conductance, read via the drain terminal (Figure 6a).

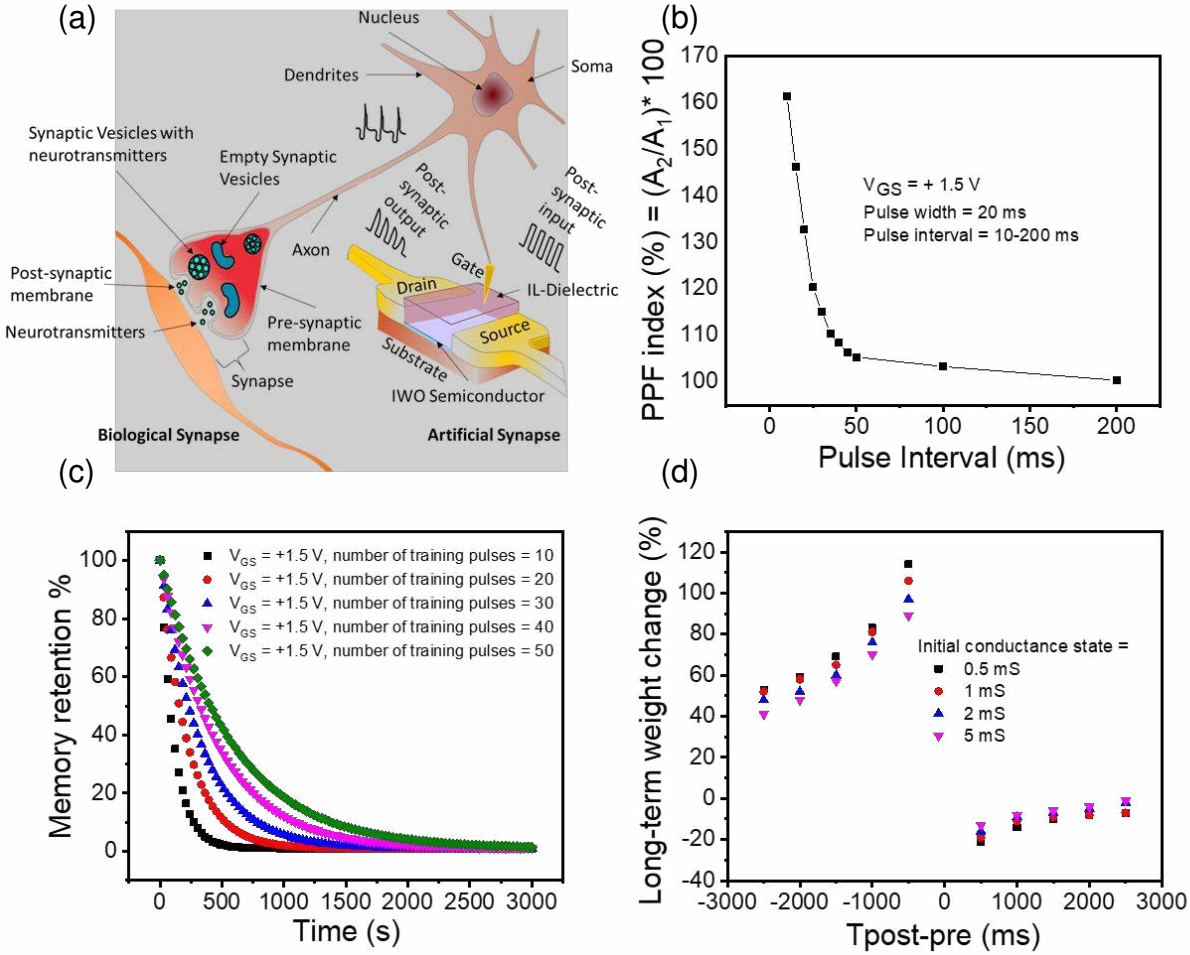

Figure 6 (a) Schematic of a biological synapse and an artificial synapse based on ionic liquid-gated IWO-based electric-double-layer (EDL) transistor. (b) PPF index as a function of pulse interval reflecting the ion migration-relaxation dynamics at the semiconductor–dielectric interface (c) Memory retention behavior as a function of number of presynaptic pulses following a trend defined by Ebbinghaus's forgetting curve. (d) Spike-timing-dependent-plasticity (STDP) with respect to various conductance states.

Classified based on the timescales of operation, short and long-term plasticity rules[38,39] defining learning and memory were studied by recording excitatory post synaptic currents (EPSCs)[40] in response to pre- and post-synaptic training sequences. A single pulse of (+ 1.5 V, 20 ms) at the gate terminal evoked a pulsed response of drain current (called Excitatory post

synaptic current (EPSC)) of 12.4 μA, which decayed back to its resting level of ~ 10 nA on removal of the presynaptic pulse (Figure S9a). A paired-pulse activation resulted in higher secondary EPSCs with an exponential dependence on the pulse interval between the spikes, resembling a phenomenon called Paired-pulse facilitation (PPF). The PPF indices were strong (>> 100 %) for small pulse intervals (< 25 ms) and weakened with increasing pulse intervals up to 200 ms, indicating a strong temporal dependence (Figure 6b, S9b). The maximum PPF index of ~ 161% was observed for a pulse interval of ~ 10 ms. This ratio decreased with increasing pulse interval and finally reached around 100 % for the largest pulse interval of 200 ms. In resemblance to the coupling of biological neurons, PPF variation with pulse interval fit well with an exponential decay function as shown below.

$$y = B_1 * \exp\left(-\frac{x}{t_1}\right) + y_0$$

where x is pulse interval time, y_0 is resting facilitation magnitude, B_1 is the facilitation constant, and t_1 is the characteristic time constant of decay phase. Detailed comparison of the decay time constants is presented in Table T1 below. In all the above measurements, short nature of the training sequences resulted in the decay of post-synaptic currents (PSCs) back to the initial state due to ion relaxation mechanisms, analogous to short-term plasticity.[41] With the ionic top-gated TFTs operating at 0.01 V (V_{ds}), the power consumption was calculated to be ~ 2.5 nJ per synaptic event (calculated from peak value of the 1st EPSC) for the best-performing devices.

Table T1: Best fit values of PPF decay as a function of pulse interval

Mode	y0	A1	t1	Reduced Chi-Sqr	R-Square(COD)	Adj. R-Square
ExpDec1	101.42957	126.4018	13.78752	2.29455	0.99525	0.99406

Persistent training consolidated the weight changes, leading to precisely controlled non-volatile changes in channel-conductance, emulating long-term plasticity features.[38,42] Application of 10 excitatory (+ 1.5 V) and inhibitory (- 1.5 V) pulses of pulse width 500 ms resulted in a non-volatile weight potentiation of 114 % and depression of 22 % starting from the same initial conductance state of 0.5 mS (Figure S10). For long-term weight analysis the following approach was used in the manuscript throughout.

(i) Read the channel conductance with V_{ds} = 0.1 V.

(ii)Apply necessary voltage waveforms to induce non-volatile weight change/ long-term plasticity.

(iii) Monitor the channel conductance 30 minutes after application of the waveforms and compare it to the initial conductance state to calculate weight %.

Directly proportional to the number, duration and amplitude of the training pulses, these devices depicted enhanced learning rate and memory retention with repetitive training sequences as depicted by Ebbinghaus's forgetting curves (Figure 6c). Spaced repetition resulted in softening of the downward slope of the forgetting curve, indicating modulation of the strength of memory and process of forgetting that occurs with the passage of time. Next, spike-based computing rules, also known as spike timing dependent plasticity (STDP) rules were emulated in these devices with the gate and source terminals acting as pre- and post-synaptic terminals and the drain terminal probing the change in channel conductance/weight. A refinement of Hebb's theory, STDP is considered to be the first law of synaptic plasticity and is believed to underlie learning and memory in neural networks.[43] In glutamatergic connections, strengthening/LTP occurs if the presynaptic spike precedes the post-synaptic spike ($t_{post-pre} > 0$, where δt is the relative time interval between the pre- and post-synaptic spikes), while presynaptic spikes following post-synaptic spikes ($t_{post-pre} < 0$) causes weakening/LTD. In these devices, spike patterns corresponding to Figure S11 created interval-dependant net voltage changes across the device, resulting in temporally manipulatable weight changes following an asymmetric anti-Hebbian rule (Figure 6d). For example, an interval ($t_{post-pre}$) of + 500 ms resulted in a net voltage of V_{pre}-V_{post} = (-0.75) – (+0.75) = - 1.5 V developed across the device, triggering a permanent decrease in the channel conductance or LTD (~ 22 %). On arrival of presynaptic pulses after postsynaptic pulses, i.e. $t_{post-pre}$ of - 500 ms, the maximum net voltage developed across the device was V_{pre}-V_{post} = (+ 0.75) – (- 0.75) = + 1.5 V and this resulted in an increase in conductance or LTP (~ 114 %). These measurements were repeated for several combinations of spike intervals and the weight changes were plotted as a function of $t_{post-pre}$ as shown in Figure S12. Weight changes were predominant at small pulse intervals, and weakened with increase in the interval, reflecting strong temporal correlations between the pre- and post-synaptic spikes. Interestingly, the magnitude of weight changes depicted a strong dependence on the initial channel concentration as shown in Figure 6d. Devices with a lower initial channel conductance (0.5 mS, read at + 0.1 V) depicted larger weight changes compared to devices in the depletion-mode with a higher initial channel conductance (5 mS) for all temporal correlations between pre- and post-synaptic spikes. This

priming-like activity enhances the programmability of these artificial synapses, paving way for highly-plastic neuromorphic circuits.[35]

These non-volatile changes in conductance correlate to the creation of additional oxygen vacancies in the semiconducting channel, as detailed in the initial sections of this study. Persistent stressing of the gate terminal with positive training pulses facilitate extraction of oxygen (creation of oxygen vacancies) from the semiconducting lattice to generate additional carriers for charge transport, resulting in a permanent shift of V_{th} and a long-term increase in channel conductance or in other words long-term potentiation. Higher electric fields or larger number of rehearsals (training pulses) accelerate this extraction process, shifting the channel conductance by larger amounts, as depicted by the Ebbinghaus forgetting curves and strong temporal dependence of the STDP curves. Application of electric field in the opposite direction (negative biasing) intercalates oxygen back into the semiconducting channel, shifting the electrical parameters back to their original state and hence, causing long-term depression. The higher barrier for intercalation is again reflected by the lower numerical value of the depression indices in the STDP curve (Figure 6d).

Conclusion:

In conclusion, field-driven athermal activation of AMOS is established comprehensively as a promising alternative to conventional high-temperature annealing techniques, enabling facile fabrication of flexible oxide electronics. Dependent on the magnitude of electric field and measurement ambient, detailed device parameter and spectroscopic analyses reveal the role of ionic liquid as an effective surface-defect passivator and an oxygen-getter, altering the oxygen stoichiometry/local electronic structure of AMOS athermally. This not only enables selective activation of oxygen-compensated thin films without the need of high-temperature processing, but also allows precise control over the carrier concentration and threshold voltage of active devices, facilitating on-demand programming of logic circuits and neuromorphic transistors. Also, the initially non-functioning TFT was activated to a working transistor with mobility of 7.1 $cm^2V^{-1}s^{-1}$ and on-off ratio of 10^6. High-performance ionic gated transistors with mobility of 105.4 cm^2/Vs were realized on flexible substrates using this technique at room temperature. Active modulation of the operational modes (enhancement and depletion) allowed facile implementation of logic inverters. Finally, precise control of these conductance changes via active generation/depletion of oxygen vacancies were portrayed as synaptic weight changes in

a neuromorphic TFT configuration, paving way for ultrafast high-performance bio-inspired spike-based computing circuits.

Experimental Procedure:

Device fabrication: IWO thin films (thickness ~7 nm) were deposited on SiO_2/Si wafers at room temperature using a RF magnetron sputtering technique with a In_2O_3:WO_3 (a-IWO) (98 : 2 wt%) target (99.99% purity from Kurt J. Lesker) at a constant chamber pressure of 5 mtorr and RF power of 50W. The flow rate of O_2 bleeder gas was varied from 1 to 3 sccm, at a Ar flow rate of 20 sccm to vary the gas mixing ratio (Ar: O). ITO (100nm-sputtered, 5 mtorr and RF power of 50W) through shadow masks can be used to form the source and drain contacts and the devices were finally annealed at 200°C for 30min in air. The details of the fabrication for flexible TFT on Polyimide (PI) substrates are described in our previous publication[26].

Electrical Characterization: Electrical measurements were carried out in vacuum (10^{-5} mbar) in a Desert Cryogenics (Lakeshore) probe station using Keithley 4200-SCS semiconductor characterization system. The ionic liquid was pre-heated for 3 hrs at 120^{O}C in a vacuum oven to remove traces of moisture. Sample's channel areas were then laminated with ionic liquid for field-driven activation and its associated measurements. To probe the extent of oxygen extraction in the semiconducting channel, all traces of ionic liquid was thoroughly removed from the substrate surface (by ultrasonication with DI water, acetone and isopropyl alcohol, followed by drying with N_2 gas) prior to back-gated FET measurements. The measurements in different ambient were carried out by bleeding Ar, N_2 and dry air respectively into the vacuum measurement chamber at a pressure of 30psi.

Physical characterization:

Surface morphology of anneal vs unannealed IWO films on SiO2 / Si were analyzed by AFM measurement (AFM Asylum Research Cypher S). X-ray photoelectron spectroscopy (XPS) measurements were obtained by a Kratos AXIS Supra XPS that is equipped with an automated dual anode (Al Kα) X-ray monochromatic source. (the source Al Kα 1486.6eV) at pressure of 5 × 10−8 torr (UHV). The films were fitted well with three Gaussian curves using multiple peaks similar to the fitting done in recent work[26]. XRD pattern of 50 nm thick IWO layer annealed at 200°C was collected by X-ray diffraction (GIXRD) (Bruker D8 Advance Diffractometer).

Associated Content

Supporting Information

The Supporting Information is available free of charge on the ACS Publications website.

AFM images, XRD of IWO thin film, Variation in transfer characteristics with respect to various Drain bias voltages, Effect of of ionic liquid gating with positive and negative biasing voltage on the transfer characteristics of IWO TFT (effect of Synthetic air), normalized change in drain current with respect to oxygen partial pressure, Effect of vaccum and various gaseous environments and respective transfer characteristics, Effect of biasing time on backgated TFT, comparison between input output characteristics of inverter in vacuum and synthetic air, Synapse: epsc, PPF, excitatory- inhibitory pulses, LTP, LTD, Input spike pattern.

Author Information

Corresponding Author

*Email: Nripan@ntu.edu.sg

Author Contributions

M.R.K, RA.J. and N.M. conceived the project and experimental flow. M.R.K. fabricated the devices, performed the experiments, and analysed the data, with help of N.T., R.A.J., A.N. and A.C.N.. M.R.K., RA.J. and N.M. wrote the manuscript with input from all authors.

Notes

The authors declare no competing financial interest.

Acknowledgements

The authors would like to acknowledge the funding from MOE Tier 1 grants RG 166/16 and MOE Tier 2 grant MOE2016-T2-1-100. Authors would like to acknowledge Tay Ying Fan for his valuable assistance XPS analysis.

References:

(1) Nomura, K.; Ohta, H.; Takagi, A.; Kamiya, T.; Hirano, M.; Hosono, H. Room-Temperature Fabrication of Transparent Flexible Thin-Film Transistors Using Amorphous Oxide Semiconductors. *Nature* **2004**, *432* (7016), 488. https://doi.org/10.1038/nature03090.

(2) Kamiya, T.; Hosono, H. Material Characteristics and Applications of Transparent Amorphous Oxide Semiconductors. *NPG Asia Mater.* **2010**, *2* (1), 15–22. https://doi.org/10.1038/asiamat.2010.5.

(3) Fortunato, E.; Barquinha, P.; Martins, R. Oxide Semiconductor Thin-film Transistors: A Review of Recent Advances. *Adv. Mater.* **2012**, *24* (22), 2945–2986.

(4) Hosono, H. Ionic Amorphous Oxide Semiconductors: Material Design, Carrier Transport, and Device Application. *J. Non. Cryst. Solids* **2006**, *352* (9–20 SPEC. ISS.), 851–858. https://doi.org/10.1016/j.jnoncrysol.2006.01.073.

(5) Iwasaki, T.; Itagaki, N.; Den, T.; Kumomi, H.; Nomura, K.; Kamiya, T.; Hosono, H. Combinatorial Approach to Thin-Film Transistors Using Multicomponent Semiconductor Channels: An Application to Amorphous Oxide Semiconductors in In–Ga–Zn–O System. *Appl. Phys. Lett.* **2007**, *90* (24), 242114.

(6) John, R. A.; Nguyen, A. C.; Chen, Y.; Shukla, S.; Chen, S.; Mathews, N. Modulating Cationic Ratios for High-Performance Transparent Solution-Processed Electronics. *ACS Appl. Mater. Interfaces* **2016**, *8* (2), 1139–1146. https://doi.org/10.1021/acsami.5b08880.

(7) Jeong, S.; Ha, Y.; Moon, J.; Facchetti, A.; Marks, T. J. Role of Gallium Doping in Dramatically Lowering Amorphous-oxide Processing Temperatures for Solution-derived Indium Zinc Oxide Thin-film Transistors. *Adv. Mater.* **2010**, *22* (12), 1346–1350.

(8) Park, J. S.; Maeng, W.-J.; Kim, H.-S.; Park, J.-S. Review of Recent Developments in Amorphous Oxide Semiconductor Thin-Film Transistor Devices. *Thin Solid Films* **2012**, *520* (6), 1679–1693.

(9) Kim, M. G.; Kanatzidis, M. G.; Facchetti, A.; Marks, T. J. Low-Temperature Fabrication of High-Performance Metal Oxide Thin-Film Electronics via Combustion Processing. *Nat. Mater.* **2011**, *10* (5), 382–388. https://doi.org/10.1038/nmat3011.

(10) Wang, B.; Zeng, L.; Huang, W.; Melkonyan, F. S.; Sheets, W. C.; Chi, L.; Bedzyk, M. J.; Marks, T. J.; Facchetti, A. Carbohydrate-Assisted Combustion Synthesis to Realize High-Performance Oxide Transistors. *J. Am. Chem. Soc.* **2016**, *138* (22), 7067–7074. https://doi.org/10.1021/jacs.6b02309.

(11) Kim, Y.-H.; Heo, J.-S.; Kim, T.-H.; Park, S.; Yoon, M.-H.; Kim, J.; Oh, M. S.; Yi, G.-R.; Noh, Y.-Y.; Park, S. K. Flexible Metal-Oxide Devices Made by Room-Temperature Photochemical Activation of Sol-Gel Films. *Nature* **2012**, *489* (7414), 128–132.

(12) John, R. A.; Chien, N. A.; Shukla, S.; Tiwari, N.; Shi, C.; Ing, N. G.; Mathews, N. Low-Temperature Chemical Transformations for High-Performance Solution-Processed Oxide Transistors. *Chem. Mater.* **2016**, *28* (22), 8305–8313. https://doi.org/10.1021/acs.chemmater.6b03499.

(13) Ueno, K.; Nakamura, S.; Shimotani, H.; Yuan, H. T.; Kimura, N.; Nojima, T.; Aoki, H.; Iwasa, Y.; Kawasaki, M. Discovery of Superconductivity in KTaO 3 by Electrostatic Carrier Doping. *Nat. Nanotechnol.* **2011**, *6* (7), 408. https://doi.org/10.1038/nnano.2011.78.

(14) Gallagher, P.; Lee, M.; Petach, T. A.; Stanwyck, S. W.; Williams, J. R.; Watanabe, K.; Taniguchi, T.; Goldhaber-Gordon, D. A High-Mobility Electronic System at an Electrolyte-Gated Oxide Surface. *Nat. Commun.* **2015**, *6*, 6437.

(15) Ye, J. T.; Inoue, S.; Kobayashi, K.; Kasahara, Y.; Yuan, H. T.; Shimotani, H.; Iwasa, Y. Liquid-Gated Interface Superconductivity on an Atomically Flat Film. *Nat. Mater.* **2010**, *9* (2), 125–128. https://doi.org/10.1038/nmat2587.

(16) Jeong, J.; Aetukuri, N. B.; Passarello, D.; Conradson, S. D.; Samant, M. G. In a Correlated-Electron Insulator Induced by Ionic Liquid Gating. **2015**, *112* (4). https://doi.org/10.1073/pnas.1419051112.

(17) Wang, Y.; Xiao, J.; Zhu, H.; Li, Y.; Alsaid, Y.; Fong, K. Y.; Zhou, Y.; Wang, S.; Shi, W.; Wang, Y.; et al. Structural Phase Transition in Monolayer MoTe 2 Driven by Electrostatic Doping. *Nature* **2017**, *550* (7677), 487.

(18) Lu, N.; Zhang, P.; Zhang, Q.; Qiao, R.; He, Q.; Li, H.-B.; Wang, Y.; Guo, J.; Zhang, D.; Duan, Z.; et al. Electric-Field Control of Tri-State Phase Transformation with a Selective Dual-Ion Switch. *Nature* **2017**, *546* (7656), 124.

(19) Sayago, J.; Meng, X.; Quenneville, F.; Liang, S.; Bourbeau, É.; Soavi, F.; Cicoira, F.; Santato, C. Electrolyte-Gated Polymer Thin Film Transistors Making Use of Ionic Liquids and Ionic Liquid-Solvent Mixtures. *J. Appl. Phys.* **2015**, *117* (11), 112809. https://doi.org/10.1063/1.4913835.

(20) Lee, J.; Kaake, L. G.; Cho, J. H.; Zhu, X.-Y.; Lodge, T. P.; Frisbie, C. D. Ion Gel-Gated Polymer Thin-Film Transistors: Operating Mechanism and Characterization of Gate Dielectric Capacitance, Switching Speed, and Stability. *J. Phys. Chem. C* **2009**, *113* (20), 8972–8981. https://doi.org/10.1021/jp901426e.

(21) Béguin, F.; Raymundo-Piñero, E.; Frackowiak, E. Electrical Double-Layer Capacitors and Pseudocapacitors; Taylor & Francis, 2009; pp 329–375. https://doi.org/10.1201/9781420055405-c8.

(22) Yang, J. J.; Strukov, D. B.; Stewart, D. R. Memristive Devices for Computing. *Nat. Nanotechnol.* **2013**, *8* (1), 13–24.

(23) Yang, J. J.; Pickett, M. D.; Li, X.; Ohlberg, D. A. A.; Stewart, D. R.; Williams, R. S. Memristive Switching Mechanism for Metal/Oxide/Metal Nanodevices. *Nat. Nanotechnol.* **2008**, *3* (7), 429.

(24) Pudasaini, P. R.; Noh, J. H.; Wong, A. T.; Ovchinnikova, O. S.; Haglund, A. V.; Dai, S.; Ward, T. Z.; Mandrus, D.; Rack, P. D. Ionic Liquid Activation of Amorphous Metal-Oxide Semiconductors for Flexible Transparent Electronic Devices. *Adv. Funct. Mater.* **2016**, *26* (17), 2820–2825. https://doi.org/10.1002/adfm.201505274.

(25) Kalhori, H.; Coey, M.; Abdolhosseini Sarsari, I.; Borisov, K.; Porter, S. B.; Atcheson, G.; Ranjbar, M.; Salamati, H.; Stamenov, P. Oxygen Vacancy in WO3 Film-Based FET with Ionic Liquid Gating. *Sci. Rep.* **2017**, *7* (1), 1–10. https://doi.org/10.1038/s41598-017-12516-y.

(26) Tiwari, N.; Rajput, M.; John, R. A.; Kulkarni, M. R.; Nguyen, A. C.; Mathews, N. Indium Tungsten Oxide Thin Films for Flexible High-Performance Transistors and Neuromorphic Electronics. *ACS Appl. Mater. Interfaces* **2018**, acsami.8b06956. https://doi.org/10.1021/acsami.8b06956.

(27) Qu, M.; Chang, C.; Meng, T.; Zhang, Q.; Liu, P.; Shieh, H. D. Stability Study of Indium Tungsten Oxide Thin-film Transistors Annealed under Various Ambient Conditions. *Phys. status solidi* **2017**, *214* (2), 1600465.

(28) Dean, J. A. *Lange' s Handbook of Chemistry*; 1999; Vol. 229. https://doi.org/10.1016/S0016-0032(40)90947-4.

(29) John, R. A.; Ko, J.; Kulkarni, M. R.; Tiwari, N.; Chien, N. A.; Geok, N.; Leong, W. L.; Mathews, N. Flexible Ionic-Electronic Hybrid Oxide Synaptic TFTs with Programmable Dynamic Plasticity for Brain-Inspired Neuromorphic Computing. *Small* **2017**, *13* (32).

(30) Tian, H.; Guo, Q.; Xie, Y.; Zhao, H.; Li, C.; Cha, J. J.; Xia, F.; Wang, H. Anisotropic Black Phosphorus Synaptic Device for Neuromorphic Applications. *Adv. Mater.* **2016**, *28* (25), 4991–4997.

(31) Zhu, L. Q.; Wan, C. J.; Guo, L. Q.; Shi, Y.; Wan, Q. Artificial Synapse Network on Inorganic Proton Conductor for Neuromorphic Systems. *Nat. Commun.* **2014**, *5*.

(32) Socratous, J.; Banger, K. K.; Vaynzof, Y.; Sadhanala, A.; Brown, A. D.; Sepe, A.; Steiner, U.; Sirringhaus, H. Electronic Structure of Low-Temperature Solution-Processed Amorphous Metal Oxide Semiconductors for Thin-Film Transistor

Applications. *Adv. Funct. Mater.* **2015**, *25* (12), 1873–1885.

(33) He, Y.; Yang, Y.; Nie, S.; Liu, R.; Wan, Q. Electric-Double-Layer Transistors for Synaptic Devices and Neuromorphic Systems. *J. Mater. Chem. C* **2018**, *6* (20), 5336–5352. https://doi.org/10.1039/C8TC00530C.

(34) Burr, G. W.; Shelby, R. M.; Sebastian, A.; Kim, S.; Kim, S.; Sidler, S.; Virwani, K.; Ishii, M.; Narayanan, P.; Fumarola, A. Neuromorphic Computing Using Non-Volatile Memory. *Adv. Phys. X* **2017**, *2* (1), 89–124.

(35) John, R. A.; Tiwari, N.; Yaoyi, C.; Ankit, *; Tiwari, N.; Kulkarni, M.; Nirmal, A.; Nguyen, A. C.; Basu, A.; Mathews, N. Ultralow Power Dual Gated Sub-Threshold Oxide Neuristors: An Enabler For Higher Order Neuronal Temporal Correlations. *ACS Nano* **2018**.

(36) Yang, J.; Ge, C.; Du, J.; Huang, H.; He, M.; Wang, C.; Lu, H.; Yang, G.; Jin, K. Artificial Synapses Emulated by an Electrolyte-Gated Tungsten-Oxide Transistor. *Adv. Mater.* **2018**, 1801548.

(37) John, R. A.; Liu, F.; Chien, N. A.; Kulkarni, M. R.; Zhu, C.; Fu, Q.; Basu, A.; Liu, Z.; Mathews, N. Synergistic Gating of Electro-Iono-Photoactive 2D Chalcogenide Neuristors: Coexistence of Hebbian and Homeostatic Synaptic Metaplasticity. *Adv. Mater.* **2018**, 1800220.

(38) Ohno, T.; Hasegawa, T.; Tsuruoka, T.; Terabe, K.; Gimzewski, J. K.; Aono, M. Short-Term Plasticity and Long-Term Potentiation Mimicked in Single Inorganic Synapses. *Nat. Mater.* **2011**, *10* (8), 591–595.

(39) Castro-Alamancos, M. A.; Connors, B. W. Short-Term Synaptic Enhancement and Long-Term Potentiation in Neocortex. *Proc. Natl. Acad. Sci.* **1996**, *93* (3), 1335–1339.

(40) Perea, G.; Araque, A. Astrocytes Potentiate Transmitter Release at Single Hippocampal Synapses. *Science (80-.).* **2007**, *317* (5841), 1083–1086.

(41) Blitz, D. M.; Foster, K. A.; Regehr, W. G. Short-Term Synaptic Plasticity: A Comparison of Two Synapses. *Nat. Rev. Neurosci.* **2004**, *5* (8), 630–640.

(42) Daoudal, G.; Debanne, D. Long-Term Plasticity of Intrinsic Excitability: Learning Rules and Mechanisms. *Learn. Mem.* **2003**, *10* (6), 456–465.

(43) Song, S.; Miller, K. D.; Abbott, L. F. Competitive Hebbian Learning through Spike-Timing-Dependent Synaptic Plasticity. *Nat. Neurosci.* **2000**, *3* (9), 919–926.